

# In Situ Deprotection of Polymeric Binders for Solution-Processible Sulfide-Based All-Solid-State Batteries

Jieun Lee, Kyulin Lee, Taegeun Lee, Hyuntae Kim, Kyungsu Kim, Woosuk Cho, Ali Coskun, Kookheon Char,\* and Jang Wook Choi\*

Sulfide-based all-solid-state batteries (ASSBs) have been featured as promising alternatives to the current lithium-ion batteries (LIBs) mainly owing to their superior safety. Nevertheless, a solution-based scalable manufacturing scheme has not yet been established because of the incompatible polarity of the binder, solvent, and sulfide electrolyte during slurry preparation. This dilemma is overcome by subjecting the acrylate (co)polymeric binders to protection–deprotection chemistry. Protection by the *tert*-butyl group allows for homogeneous dispersion of the binder in the slurry based on a relatively less polar solvent, with subsequent heat-treatment during the drying process to cleave the *tert*-butyl group. This exposes the polar carboxylic acid groups, which are then able to engage in hydrogen bonding with the active cathode material, high-nickel layered oxide. Deprotection strengthens the electrode adhesion such that the strength equals that of commercial LIB electrodes, and the key electrochemical performance parameters are improved markedly in both half-cell and full-cell settings. The present study highlights the potential of sulfide-based ASSBs for scalable manufacturing and also provides insights that protection–deprotection chemistry can generally be used for various battery cells that suffer from polarity incompatibility among multiple electrode components.

As the territory of lithium-ion batteries (LIBs) is expanding to the green transportation sector, concerns about LIBs presenting a fire hazard originating from the use of flammable carbonate solvents have been elevated.<sup>[1]</sup> All-solid-state batteries (ASSBs) are receiving considerable attention as viable alternatives to LIBs,<sup>[2]</sup> as the elimination of flammable liquid solvents

from the electrolyte would allow the safety issue to be fundamentally dismissed. Furthermore, ASSBs offer additional advantages, such as enhanced interfacial stability with Li metal electrodes and the bipolar stacking of electrodes for higher energy density.<sup>[3]</sup> Based on this motivation, various inorganic solid electrolytes (SEs) have been identified in the past decades. Among several different classes, sulfide-based SEs, including  $\text{Li}_7\text{P}_3\text{S}_{11}$ ,<sup>[2a]</sup>  $\text{Li}_{10}\text{GeP}_2\text{S}_{12}$ ,<sup>[4]</sup> and  $\text{Li}_{9.54}\text{Si}_{1.74}\text{P}_{1.44}\text{S}_{11.7}\text{Cl}_{0.3}$ ,<sup>[5]</sup> are remarkable because some of them realize high ionic conductivity of the order of  $10^{-2} \text{ S cm}^{-1}$ , which is even comparable to those of their liquid counterparts. In particular, the argyrodites  $\text{Li}_6\text{PS}_5\text{X}$  ( $\text{X} = \text{Cl, Br, and I}$ ) are of great interest by virtue of their competitive ionic conductivity at room temperature, mechanical properties that allow intimate particle-to-particle contact, ease of synthesis, and the affordability of their raw materials.<sup>[6]</sup> Despite the advantages associated with the inherent properties of these materials, ASSB technology continues to lag at the research stage because a large-scale manufacturing scheme has yet to be established. Thus far, ASSBs have been tested mainly by fabricating lab-scale pellet-type cells for which the electrode and electrolyte powder were pressed into an assembly of individual layers. Targeting large-scale production, solution-based roll-to-roll coating and drying are preferred from the perspectives of economic feasibility and mass productivity.<sup>[7]</sup> Indeed, the increasing demand for solution-based manufacturing processes for ASSBs has recently been recognized.<sup>[8]</sup> However, detailed conditions for slurry preparation and electrode fabrication are yet to be identified and optimized.


A major challenge in developing solution-processed ASSBs based on sulfide SEs lies in the difficulty of finding the right combinations of polymeric binder and slurry solvent. Critically, most sulfide SEs are soluble in polar solvents, including the most popular solvent for LIB slurries, *N*-methyl-2-pyrrolidone (NMP).<sup>[9]</sup> Hence, solvent selection is limited to nonpolar or relatively less polar solvents. This restriction on the choice of solvent consequently limits the choice of binder, implying that most polymers with polar functional groups cannot be considered.<sup>[10]</sup> More seriously, binders that are compatible with these solvents and sulfide SE pairs in terms of polarity would result

J. Lee, Dr. K. Lee, T. Lee, H. Kim, Prof. K. Char, Prof. J. W. Choi  
School of Chemical and Biological Engineering and Institute of Chemical Processes

Seoul National University  
1 Gwanak-ro, Gwanak-gu, Seoul 08826, Republic of Korea  
E-mail: khchar@snu.ac.kr; jangwookchoi@snu.ac.kr

Dr. K. Kim, Dr. W. Cho  
Advanced Batteries Research Center  
Korea Electronics Technology Institute  
25 Saenari-ro, Bundang-gu, Seongnam, Gyeonggi 13509, Republic of Korea

Prof. A. Coskun  
Department of Chemistry  
University of Fribourg  
Chemin de Musee 9, Fribourg 1700, Switzerland

 The ORCID identification number(s) for the author(s) of this article can be found under <https://doi.org/10.1002/adma.202001702>.

http://doc.rero.ch

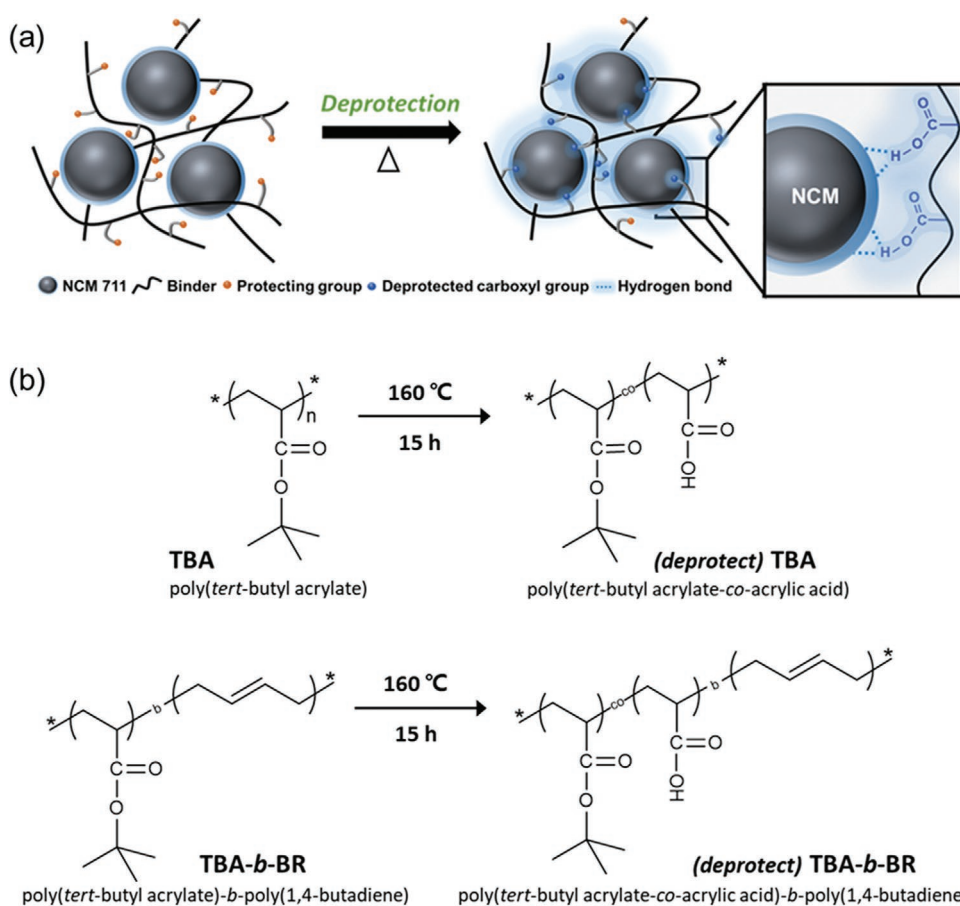


**Figure 1.** a) Schematic illustration of the protection–deprotection chemistry for the adhesive interaction between the polymeric binder and active material in the composite cathode. b) Structural changes of poly(*tert*-butyl acrylate) (TBA) and poly(*tert*-butyl acrylate)-*b*-poly(1,4-butadiene) (TBA-*b*-BR) after thermal deprotection.

in weak adhesion to the current collector or weak cohesion between active materials as well as between the active materials and SEs. The inferior mechanical properties of the resulting electrodes would result in poor processability<sup>[10]</sup> and inferior electrochemical performance represented by high interfacial resistance, capacity fading upon cycling, etc., thereby placing a severe hurdle in the way of the entire sulfide-based ASSB technology.

Because of the dilemmatic issue of the need for compatibility among the three components (solvent, binder, and SE), only nonpolar or weakly polar solvents, such as *para*(*p*)-xylene, toluene, hexane, and anisole, have been adopted together with polymeric binders with low polarities, such as butadiene rubber (BR),<sup>[8b]</sup> styrene–butadiene rubber (SBR),<sup>[8c]</sup> styrene–ethylene–butylene–styrene rubber (SEBS),<sup>[8d]</sup> poly(vinyl chloride) (PVC),<sup>[8e]</sup> nitrile butadiene rubber (NBR),<sup>[8g,11]</sup> silicone rubber,<sup>[8c]</sup> and ethyl cellulose.<sup>[8i,12]</sup> In order to overcome this challenging trade-off between the chemical compatibility and mechanical stability of the electrode, out-of-the-box approaches are a “must-need”.

Herein, we report a novel binder concept involving protection–deprotection chemistry that can alter the polarity of the binder in the course of the electrode manufacturing process, that is, during the slurry mixing stage and final electrode fabrication stage. The polar functional groups of the binder

were protected by nonpolar *tert*-butyl (*t*-butyl) groups to ensure that the polymer is compatible with the argyrodite sulfide SE, Li<sub>6</sub>PS<sub>5</sub>Cl (abbreviated as LPSCl) in the slurry mixing process. This polymer could be deprotected by thermally cleaving the *t*-butyl group during the process of drying the electrode, thus enabling a polar binder to be obtained (Figure 1a). The resulting electrode exhibited superior electrode adhesion and electrochemical properties in various respects in comparison with those of its BR counterpart, a common reference binder for solution-processed sulfide-based ASSBs. Apart from the enhanced mechanical and electrochemical properties of the ASSB cells, the current investigation opens a new avenue in battery binder designs, that is, protection–deprotection chemistries that allow the binder to transform its functionality at different stages of the cell manufacturing process.

To realize polymeric binder design based on the novel concept of protection–deprotection chemistry, we chose poly(*tert*-butyl acrylate) (TBA) and its block copolymer version, poly(*tert*-butyl acrylate)-*b*-poly(1,4-butadiene) (TBA-*b*-BR), with the carboxylic acid functional groups of both protected by thermally cleavable *t*-butyl groups. The protection scheme involving the *t*-butyl group has been used in a wide range of synthetic procedures in the polymer chemistry field because it allows certain functionalities or positions of a polymer to be protected while modifying others, thus offering “orthogonal” modification.<sup>[13]</sup>

On the other hand, it is noted that TBA is commonly used as a precursor for the synthesis of the well-known poly(acrylic acid) (PAA).<sup>[14]</sup> Although PAA is a widely used binder for LIB electrodes,<sup>[15]</sup> it is not suitable for sulfide-based ASSBs because of the polarity mismatch; the relatively high polarity of PAA makes it soluble only in polar solvents, which are highly reactive with sulfide SEs. However, by protecting the carboxylic acid group with a *t*-butyl group, the polarity of PAA can be lowered, and the resulting lower polarity of TBA and TBA-*b*-BR renders them soluble in nonpolar or weakly polar solvents. Upon exposure to heat treatment, the *t*-butyl ester group is decomposed to release isobutene and consequently yield carboxylic acid,<sup>[16]</sup> as illustrated in Figure 1b. The deprotected polymers are denoted as poly(*tert*-butyl acrylate-*co*-acrylic acid) and poly(*tert*-butyl acrylate-*co*-acrylic acid)-*b*-poly(1,4-butadiene), abbreviated as (deprotect) TBA and (deprotect) TBA-*b*-BR, respectively. Ultimately, the original TBA and TBA-*b*-BR with moderate adhesion to the NCM active material are transformed into their PAA analogs with high adhesion while being processed using existing electrode fabrication steps. Thus, the overall polymer transformation occurs in situ. To the best of our knowledge, the present study is the first to employ in situ polarity switching of a polymeric binder for ASSB electrodes.

The weight loss of the TBA and TBA-*b*-BR binders was monitored by isothermal thermogravimetric analysis (ITGA) (Figure S1a,b, Supporting Information). When maintained at a constant temperature of 120 °C, no significant change in mass was observed, whereas the weight corresponding to the *t*-butyl group was lost after 15 h when the constant temperature was raised to 160 °C. This observation indicates the presence of a threshold temperature for deprotection of the *t*-butyl group. On the other hand, differential scanning calorimetry (DSC) profiles (Figure S1c,d, Supporting Information) reveal that the glass transition temperatures of TBA and TBA-*b*-BR are around 45 °C and below 30 °C, respectively, so that both binders are in the rubbery state at the deprotection temperature of 160 °C. The chemical bonds of TBA and TBA-*b*-BR (before deprotection) and (deprotect) TBA and (deprotect) TBA-*b*-BR (after deprotection) were investigated by Fourier transform infrared spectroscopy (FT-IR) in attenuated total reflectance (ATR) mode (Figure 2a and S2a, Supporting Information). Before the exposure to heat, TBA presented strong absorption bands for *t*-butyl at 1350 and 1400 cm<sup>-1</sup> and the C=O stretching of the ester at 1730 cm<sup>-1</sup>. After thermolysis, the signature peaks of *t*-butyl at 1350 and 1400 cm<sup>-1</sup> disappeared, and the characteristic ester stretching band at 1730 cm<sup>-1</sup> broadened owing to the appearance of the carboxylic acid band at 1709 cm<sup>-1</sup> and anhydride bands at 1752 and 1804 cm<sup>-1</sup>.<sup>[17]</sup> Even when TBA was blended with the LPSCl SE, the deprotection occurred in a consistent manner (Figure S2b, Supporting Information), implying that the presence of the LPSCl SE did not perturb the deprotection reaction. When tested solely targeting binders, the TBA film exhibited far increased adhesion with the aluminum current collector after deprotection (Figure S3, Supporting Information).

In an attempt to evaluate the chemical compatibility of TBA, (deprotect) TBA, TBA-*b*-BR, and (deprotect) TBA-*b*-BR with argyrodite LPSCl SE, X-ray diffraction (XRD) and Raman analyses were conducted (Figure S4a–d, Supporting Information). In this test, the LPSCl electrolyte was immersed in the

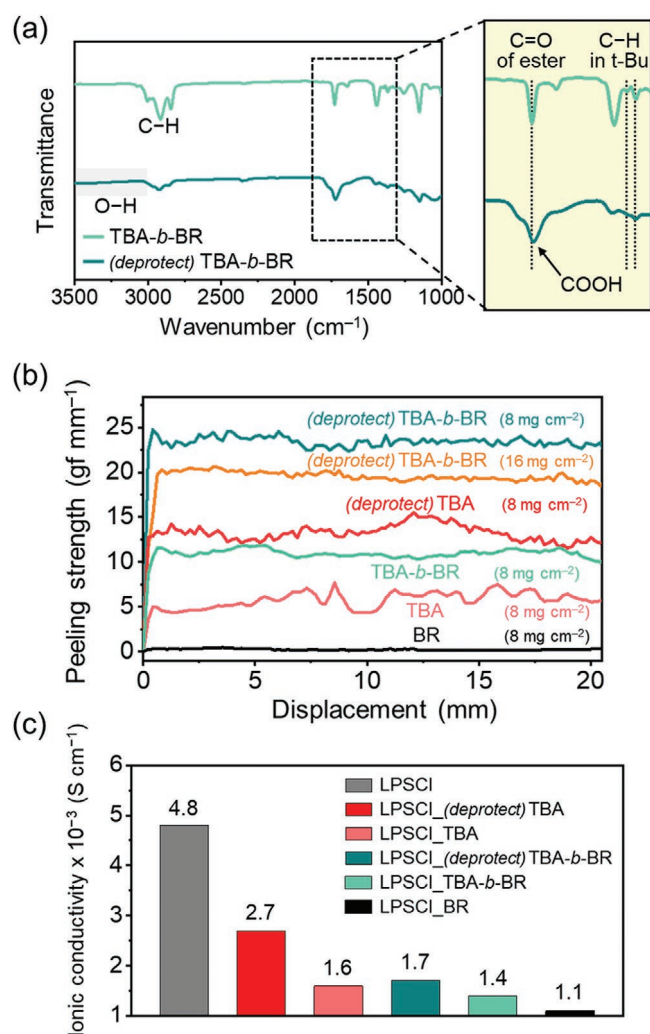


**Figure 2.** a) Fourier transform infrared spectroscopy (FT-IR) (attenuated total reflectance, ATR) spectra of the poly(*tert*-butyl acrylate)-*b*-poly(1,4-butadiene) (TBA-*b*-BR) and (deprotect) TBA-*b*-BR. b) 180° peeling test results of the electrodes containing (deprotect) TBA-*b*-BR, (deprotect) poly(*tert*-butyl acrylate) (TBA), TBA-*b*-BR, TBA, and butadiene rubber (BR) binders. c) Lithium-ion conductivities of the LPSCl solid electrolyte composite films containing (deprotect) TBA, TBA, (deprotect) TBA-*b*-BR, TBA-*b*-BR, and BR binders. LPSCl: binder = 97.5: 2.5 = w:w.

TBA and TBA-*b*-BR binder solutions based on butyl butyrate for 24 h followed by drying at 120 or 160 °C. After this treatment, the characteristic<sup>[6b,18]</sup> peaks of the LPSCl remained on the XRD pattern (Figure S4a,c, Supporting Information), and the signature peak indicative<sup>[18,19]</sup> of PS<sub>4</sub><sup>3-</sup> (422 cm<sup>-1</sup>) was also unchanged on the Raman spectra (Figure S4b,d, Supporting Information). Hence, the LPSCl SE was concluded to be chemically compatible with all the binder solutions tested herein.

Upon thermal deprotection, the 180° peeling test indicates that the (deprotect) TBA and (deprotect) TBA-*b*-BR electrodes showed far stronger adhesion compared to that of their protected versions and the bare BR electrode (Figure 2b). This test was carried out by preparing composite cathode electrodes containing 74.5 wt% of active material (LiNi<sub>0.7</sub>Co<sub>0.15</sub>Mn<sub>0.15</sub>O<sub>2</sub>, abbreviated as NCM711), 21.5 wt% of LPSCl, 2 wt% of super P,

and 2 wt% of binder with an areal NCM711 loading of 8 and 16 mg cm<sup>-2</sup>. The average peeling strength of the (deprotect) TBA-*b*-BR, (deprotect) TBA, TBA-*b*-BR, TBA and BR electrodes with a loading of 8 mg cm<sup>-2</sup> was 23.4, 13.2, 11.0, 5.81, and 0.24 gf mm<sup>-1</sup>, respectively. Also, a control experiment reveals that the peeling strength of electrodes was in proportion to the deprotection reaction time (Figure S5, Supporting Information). Remarkably, the peeling strength of the (deprotect) TBA-*b*-BR electrode was 98 times greater than that of its BR counterpart, and is even as high as that of established LIB electrodes,<sup>[8b]</sup> pointing to the feasibility of using this electrode as a high-loading electrode, which is essential for cells with commercial-level volumetric energy densities. These comparative adhesion force values, in turn, imply that the adhesion of BR binder is unsatisfactory for practical cells, despite its common use in academic research.<sup>[8b]</sup> Furthermore, the adhesive force of the (deprotect) TBA and (deprotect) TBA-*b*-BR electrodes increased nearly twice after thermal deprotection owing to the formation of hydrogen bonds between the active material and the binder. When the areal loading of NCM711 was raised to 16 mg cm<sup>-2</sup>, the (deprotect) TBA-*b*-BR electrode showed peeling strength of 19.5 gf mm<sup>-1</sup>, i.e., slightly less compared to the areal loading of 8 mg cm<sup>-2</sup>. However, this value is substantially higher than that of its (deprotect) TBA counterpart even with the low loading of 8 mg cm<sup>-2</sup> and is still extraordinarily high for sulfide-based ASSB electrodes. In addition, the enhanced peeling strength engaging the deprotection was valid for films without active material. When LPSCl films were prepared by including 10 wt% binders, LPSCl\_(deprotect) TBA showed much higher peeling strength compared to that of LPSCl\_TBA and LPSCl\_BR (Figure S6, Supporting Information) owing to the hydrogen bonds between (deprotect) TBA and the aluminum foil. On the other hand, although (deprotect) TBA has a greater proportion of carboxyl groups than (deprotect) TBA-*b*-BR, (deprotect) TBA is inherently rigid, rendering the electrode too brittle. This issue is indeed well known for acrylate type binders.<sup>[15b,20]</sup> Thus, the adhesion and chain flexibility play a synergistic role in realizing the superior adhesion of (deprotect) TBA-*b*-BR. The brittle character of the (deprotect) TBA electrode was revealed by the formation of cracks and electrode peeling when subjected to a mandrel bending test using cylindrical mandrels with different diameters (Figure S7, Supporting Information). Taking into account these two complementary properties, we chose the (deprotect) TBA-*b*-BR binder as the main binder for our electrochemical tests.

Considering the fact that the binders are ionically insulating, the effect of binder incorporation on the ionic conductivity was investigated using electrochemical impedance spectroscopy (EIS) by preparing SE composite films consisting of 97.5 wt% LPSCl SE and 2.5 wt% binder (Figure 2c). For comparison, a bare LPSCl film without binder was also prepared by cold-pressing pelletization. Significantly, the ionic conductivities of the binder-incorporated films were of the same order of magnitude, 10<sup>-3</sup> S cm<sup>-1</sup>, as that of the binder-free pelletized reference (4.8 × 10<sup>-3</sup> S cm<sup>-1</sup>), although they were exposed to the binder solutions in which the SE was immersed for 24 h. The ionic conductivities of LPSCl\_(deprotect) TBA, LPSCl\_TBA, LPSCl\_(deprotect) TBA-*b*-BR, LPSCl\_TBA-*b*-BR, and LPSCl\_BR were 2.7 × 10<sup>-3</sup>, 1.6 × 10<sup>-3</sup>, 1.7 × 10<sup>-3</sup>, 1.4 × 10<sup>-3</sup>, and 1.1 × 10<sup>-3</sup> S cm<sup>-1</sup>, respectively, implying that the LPSCl\_TBA and LPSCl\_TBA-*b*-BR films already achieved higher ionic

conductivity compared to their LPSCl\_BR counterpart and the value increased even further upon deprotection. The ionic conductivities of the binder-incorporated films indicate that all the binders were well dispersed in their slurries and electrodes because the ionic conductivities would have been impaired much more significantly if otherwise. The higher ionic conductivities of LPSCl\_(deprotect) TBA and LPSCl\_(deprotect) TBA-*b*-BR than those of LPSCl\_TBA and LPSCl\_TBA-*b*-BR can be explained by the removal of the bulky *t*-butyl group, which assists Li ion transport as a result of improved contact among the LPSCl particles. In addition, the activation energy of Li ion transport was derived from Arrhenius plots attained from ion conductivity measurements at different temperatures (25–65 °C) (Figure S8, Supporting Information). The activation energies of LPSCl\_(deprotect) TBA, LPSCl\_TBA, LPSCl\_(deprotect) TBA-*b*-BR, LPSCl\_TBA-*b*-BR, and LPSCl\_BR turned out to be 0.297, 0.365, 0.397, 0.438, and 0.473 eV, respectively, implying that upon deprotection, the ionic transport becomes less temperature sensitive.

The effect of the binder on the electrochemical performance was evaluated by fabricating all-solid-state half-cells consisting of a binder-incorporated composite cathode, binder-free LPSCl SE layer, and lithium–indium (Li–In) counter electrode (Figure 3). In this half-cell study, binder was excluded from the LPSCl SE layer to enable us to focus on the effect of the binder on the performance of the cathode. To confirm the electrochemical stability, a cyclic voltammetry (CV) test was carried out for (deprotect) TBA-*b*-BR at 0.1 mV s<sup>-1</sup> in the potential range of 1.5–3.7 V versus Li–In (Figure S9, Supporting Information). The CV profiles remained peak-free during cycling, and we thus conclude that (deprotect) TBA-*b*-BR is electrochemically stable in the given potential range. For the half-cell tests, the composite cathodes had a composition of NCM711/LPSCl/super P/binder = 74.5:21.5:2:2 by weight, and the areal mass loading of the active material was 8 or 16 mg cm<sup>-2</sup>. Once the slurry was cast on aluminum (Al) foil and dried, cell assembly was completed by cold pressing the assembled cathode, electrolyte, and anode layers. Galvanostatic scans were recorded at 0.1C (19.5 mA g<sup>-1</sup>) in the range of 1.88–3.68 V versus Li–In. Half-cells with cathodes with the lower active loading with (deprotect) TBA-*b*-BR, TBA-*b*-BR, (deprotect) TBA, TBA, and BR showed the first discharge capacities of 160.3, 160.2, 159.6, 152.8, and 160.1 mAh g<sup>-1</sup>, respectively (Figure S10a–e, Supporting Information). After 75 cycles, these (deprotect) TBA-*b*-BR, TBA-*b*-BR, (deprotect) TBA, TBA and BR cells maintained distinct specific capacities of 140.4, 62.7, 118.4, 39.9, and 29.5 mAh g<sup>-1</sup>, respectively (Figure 3a and S10, Supporting Information), corresponding to 87.6, 39.2, 74.2, 26.1, and 18.4% capacity retention with respect to their initial capacities (Figure S10f, Supporting Information). As displayed in Figure 3a, the capacity of the (deprotect) TBA-*b*-BR cell delivered cycling performance far superior to that of its protected counterpart and other binder-based cells. Notably, the trend of the cyclability is consistent with that of the electrode adhesion displayed in Figure 2b, implying that the mechanical integrity represented by the interparticle contact plays a central role in the long-term performance of the electrodes. Interestingly, cell-to-cell variations in the Coulombic efficiency (CE) were observed in the early cycling period (Figure S10g, Supporting Information) such that it is difficult to define the best binder. This phenomenon is ascribed to the well-known structural

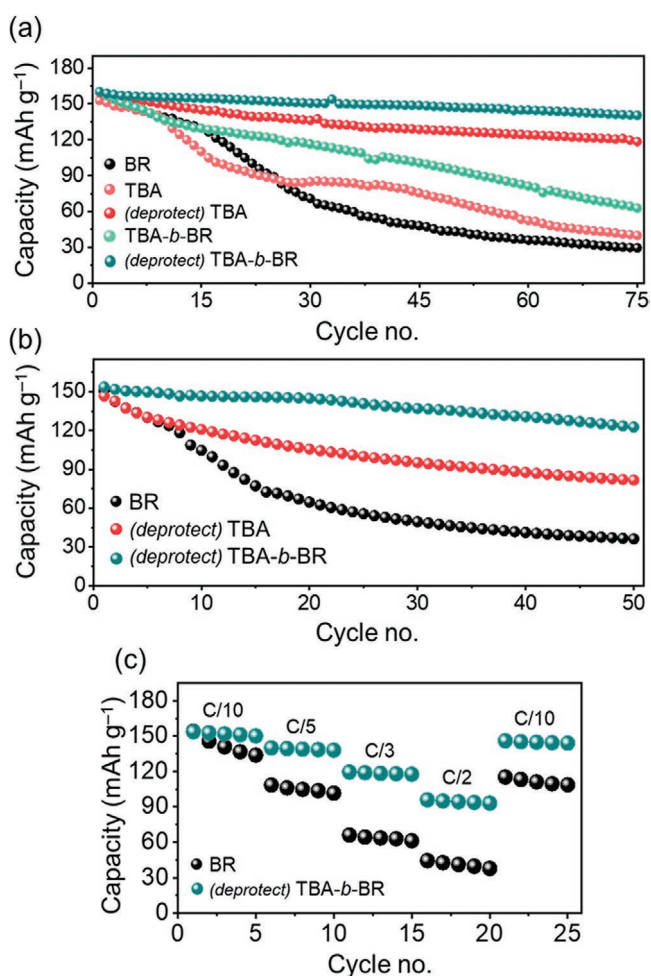


**Figure 3.** a) Cycling performance of the NCM/Li-In all-solid-state half-cells containing butadiene rubber (BR), poly(*tert*-butyl acrylate) (TBA), (deprotect) TBA, poly(*tert*-butyl acrylate)-*b*-poly(1,4-butadiene) (TBA-*b*-BR), and (deprotect) TBA-*b*-BR binders when measured at 0.1C (19.5 mA g<sup>-1</sup>) and 25 °C. Areal loading of NCM711 active material = 8 mg cm<sup>-2</sup>. b) Cycling performance of the NCM/Li-In all-solid-state half-cells containing BR, (deprotect) TBA, and (deprotect) TBA-*b*-BR binders when tested at 0.1C (19.5 mA g<sup>-1</sup>) and 25 °C. Areal loading of NCM711 active material = 16 mg cm<sup>-2</sup>. c) Rate capability of the same two cells with the loading of NCM711 active material being 16 mg cm<sup>-2</sup> when measured at various C-rates.

instability of sulfide-based SEs at high voltages that is prominent in early cycling.<sup>[21]</sup> However, in the later cycles when the SE is structurally stabilized, the CEs of the (deprotect) TBA-*b*-BR cell were more stable at high values compared to those of the other cells (Figure S10h, Supporting Information), which is once again ascribed to the strengthened interparticle contacts.

When the areal active loading was increased to 16 mg cm<sup>-2</sup>, the effect of the binder became more distinct (Figure 3b). For the half-cells with the high cathode loading, the (deprotect) TBA-*b*-BR, (deprotect) TBA, and BR half-cells exhibited initial discharge capacities of 153.5, 147.6, and 150.7 mAh g<sup>-1</sup>, respectively (Figure S11a–c, Supporting Information). With this increased areal loading, the (deprotect) TBA and BR cells clearly performed worse compared to the cells with the lower loading as both cells lost their capacities from the very early cycles and retained only 55.7% and 24.0% of their respective

initial capacities after 50 cycles. In sharp contrast, the cycling behavior of the (deprotect) TBA-*b*-BR cell with this high active loading remained comparable to that of the lower loading case, i.e., 80.0% retention after 50 cycles. Consistent with the series of results above, the superior cycling performance of the (deprotect) TBA-*b*-BR cell is largely associated with the strengthened mechanical stability of the electrode resulting from the intimate particle-to-particle contact, which also contributes to stabilizing the interface.<sup>[22]</sup> The distinct cyclability of the (deprotect) TBA-*b*-BR cell was reflected in its CEs. As recognized commonly for sulfide-based ASSBs,<sup>[23]</sup> all three of the cells adversely experienced relatively low initial CEs (76.3, 73.3, and 67.8%, respectively) due to the known thermodynamically unstable nature of LPSCl at high voltages,<sup>[21]</sup> which lead to the formation of a passivation layer on the SE. Nevertheless, the CE of the (deprotect) TBA-*b*-BR cell increased more rapidly from the 2nd cycle compared to those of the other two cells (Figure S11d, Supporting Information). The improved interparticle contact of the (deprotect) TBA-*b*-BR cell was also reflected in its superior rate performance compared to the BR cell when evaluated at C-rates ranging from 0.1 to 0.5C (Figure 3c).

In an attempt to monitor the electrochemical behavior, EIS analysis was carried out for the (deprotect) TBA-*b*-BR and BR half-cells before cycling and after 50 cycles (Figure 4). The

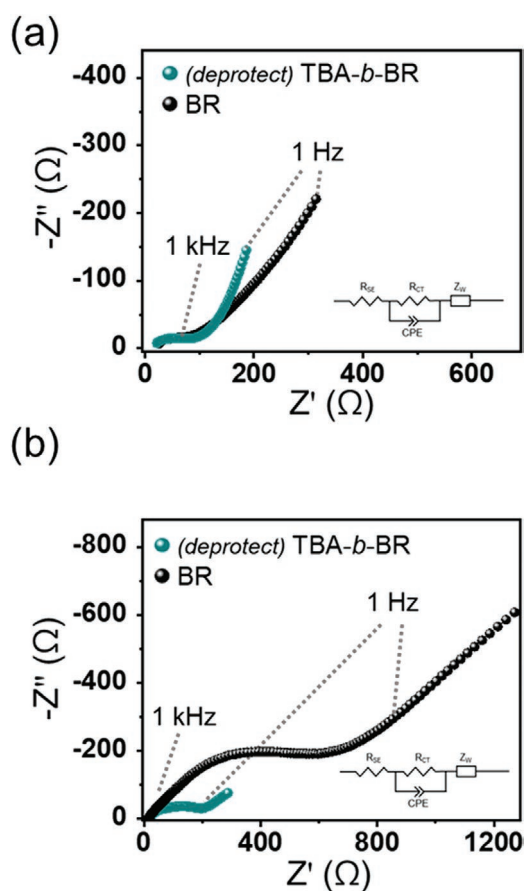


**Figure 4.** Electrochemical impedance spectroscopy (EIS) plots of the NCM/Li-In all-solid-state half-cells containing butadiene rubber (BR) and (deprotect) poly(*tert*-butyl acrylate)-*b*-poly(1,4-butadiene) (TBA-*b*-BR) binders a) before cycling and b) after 50 charge–discharge cycles at 0.1C.

electrochemical behavior was fitted to an equivalent circuit (inset in Figure 4), which made it possible to obtain the resistance of the SE layer ( $R_{SE}$ ) and the charge transfer resistance ( $R_{CT}$ ) from the  $x$ -axis intercept and the amplitude of the semicircles in the Nyquist plots, respectively.<sup>[8e,24]</sup> The  $R_{SE}$  of all samples remained similarly near  $10 \Omega \text{ cm}^2$  regardless of the cycle number, which can be interpreted to indicate that  $R_{SE}$  consistently represents the intrinsic bulk resistance of the LPSCl. In contrast, the  $R_{CT}$  of these cells increased significantly during cycling. Nonetheless, between both cells, the increase in  $R_{CT}$  was more prominent with the BR cell than with the (deprotect) TBA-*b*-BR cell; the  $R_{CT}$  of the BR cell increased from 62.2 to 508.5  $\Omega \text{ cm}^2$  after 50 cycles, whereas that of the (deprotect) TBA-*b*-BR cell increased from 54.0 to 1473  $\Omega \text{ cm}^2$ . The more significant increase in the  $R_{CT}$  of the BR cell, once again, reflects loosened interparticle contact upon cycling.

The distinct evolution of the interfacial resistance of both cells was anticipated to originate from the stability of interparticle contact during cycling. To confirm this scenario, the microstructures of the cathode composite layers were visualized before and after charge–discharge cycles using cross-sectional scanning electron microscopy (SEM) (Figure 5 and Figure S12, Supporting Information). Prior to the cycling, all of the electrodes showed intimate interparticle contact and negligible voids (Figure 5a,b and Figure S12a, Supporting Information). After 25 cycles, the most discernible feature was the formation of cracks in the active NCM711 particles; in the case of the (deprotect) TBA-*b*-BR electrode, the majority of active particles appeared to be crack-free (Figure 5c), whereas the active

particles in the BR electrode exhibited a greater number of internal cracks as marked with yellow dotted lines in Figure 5d. The formation of these cracks is a well-known degradation mechanism of the high-Ni NCM family, with its origins in the anisotropic volume expansion of the active phase.<sup>[25]</sup> Apart from this, according to the same SEM image, disintegration of the NCM711 and SE particles was more severe in the BR electrode, as indicated by the green arrows. The worsened condition of the active-SE contacts represents<sup>[26]</sup> disconnected percolation paths for Li ion transport, which also explains the larger semicircle in the EIS profile of the BR electrode after 50 cycles (Figure 4b). The loosened interparticle contact as well as the interfacial degradation during cycling is an inherently problematic aspect of ASSBs,<sup>[21d,27]</sup> although it is almost inevitable once the active material undergoes substantial volume change. All in all, stable interparticle contact resulting from enhanced adhesion of the binder plays a critical role in improving the cyclability of ASSBs, in addition to providing feasibility for large-scale processing.

Finally, our electrochemical assessment was expanded to test full-cells paired with graphite anodes. These NCM/graphite all-solid-state full-cells were fabricated by sequentially casting the composite cathode and electrolyte layers on Al foil via the doctor blade technique. The compositions of the cathode and SE layers were NCM711:LPSCl:super P:binder = 74.5:21.5:2:2 and LPSCl:binder = 97.5:2.5 in weight, respectively. The anode layer was also prepared via the same slurry casting process on nickel (Ni) foil and consisted of graphite, LPSCl, and binder in a weight ratio of 78:19.5:2.5. For the anodes,

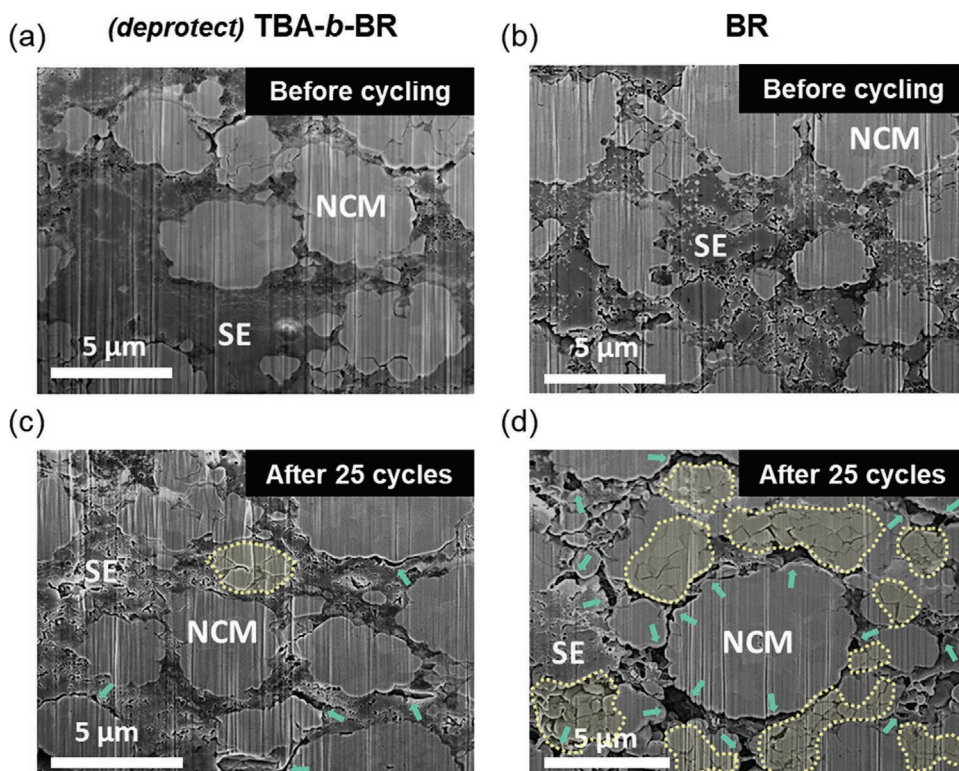


**Figure 5.** a–d) Cross-sectional scanning electron microscopy (SEM) images of the composite cathode layers containing (deprotect) poly(*tert*-butyl acrylate)-*b*-poly(1,4-butadiene) (TBA-*b*-BR) (a,c) and butadiene rubber (BR) (b,d) binders. Before cycling (a,b) and after 25 charge–discharge cycles at 0.1C (c,d).

BR binder was used because the hydrophobic nature of the graphite surface would not benefit from the binder design used for the cathode. The separately prepared cathode/SE layers and the anode layer were assembled via cold pressing to complete the full-cell. See the cross-section of the full-cell using plasma focused ion beam (FIB, Figure S13, Supporting Information). The n/p ratio, defined as the total capacity ratio between the negative and positive electrodes, was 1.2. We invoked high NCM711 loadings of  $16 \text{ mg cm}^{-2}$  to determine the practical viability of the present cell fabrication scheme involving the new binder. When cycled at 0.1C ( $19.5 \text{ mA g}_{\text{NCM}}^{-1}$ ) in the voltage range of 2.5–4.3 V (Figure 6a), the (deprotect) TBA-*b*-BR cell delivered reversible capacity of  $153.4 \text{ mAh g}_{\text{NCM}}^{-1}$  in its first cycle and retained 85.5% of the initial capacity after 45 cycles (Figure 6b). Remarkably, the CE of this full-cell reached 99.5% at the 8<sup>th</sup> cycle and stayed above this value in the subsequent cycles (inset in Figure 6b). A control full-cell based on BR binder exhibited inferior capacity retention of only 42.8% after 30 cycles (Figure S14, Supporting Information). As mentioned for the performance of the half-cells, stable cycling in the full-cell operation is attributed to increased and stable interparticle contact facilitated by enhanced adhesion of the binder.

In summary, we introduced a novel binder design based on protection–deprotection chemistry, which resolves the tricky issue of polarity compatibility among the three electrode components (solvent, binder, and SE) in the slurry solution. This task was accomplished by switching the polarity of the binder during the course of electrode fabrication via cleavage of the *t*-butyl protecting group. Upon deprotection, the polar carboxylic acid group is exposed, which enables hydrogen bonding interaction with the NCM active material to enhance the adhesion strength drastically, even beyond the levels of established LIB electrodes. When examined in both all-solid-state half-cells and full-cell settings, the (deprotect) TBA-*b*-BR cell exhibited superior cycling and rate performance compared to that of the BR and its protected analog, revealing the critical role of the deprotection scheme in the key cell performance parameters. The improved electrochemical and adhesion properties are ascribed to tightened interparticle contact and the resulting improved interfacial stability. The present investigation is the first demonstration of in situ polarity switching of the polymeric binder for solution-processible sulfide-based ASSBs and highlights the unique and useful nature of deprotection chemistry when designing binders that need to be employed in combination with multiple slurry components with incompatible polarities.

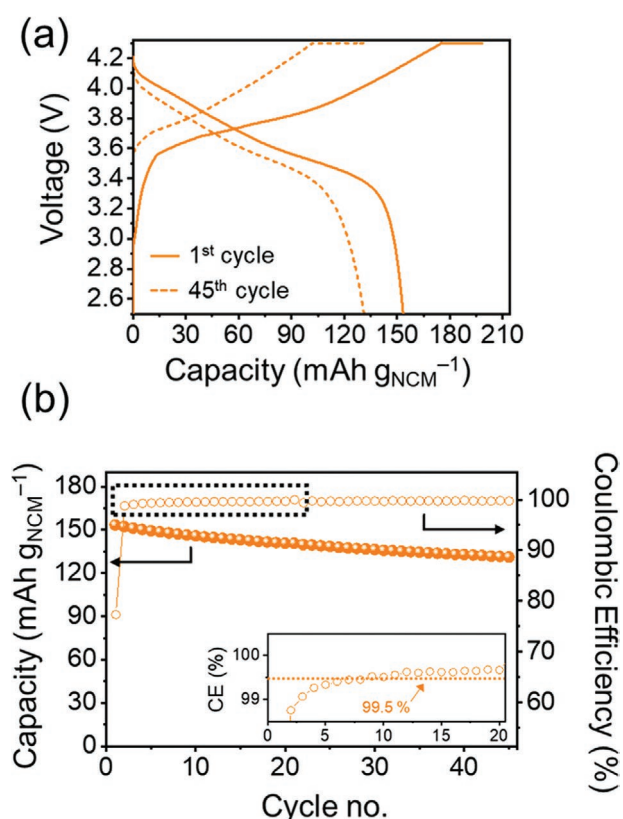


**Figure 6.** a) The 1st and 45th charge–discharge profiles of the NCM/graphite all-solid-state full-cell containing (deprotect) poly(*tert*-butyl acrylate)-*b*-poly(1,4-butadiene) (TBA-*b*-BR) binder at 0.1C ( $19.5 \text{ mA g}_{\text{NCM}}^{-1}$ ) at 25 °C. Areal loading of NCM711 active material =  $16 \text{ mg cm}^{-2}$ . b) Cycling performance and Coulombic efficiencies of the same full-cell in (a) when measured at 0.1C for both charge and discharge.

## Experimental Section

**Materials:** The argyrodite LPSCI used was bi-modal in terms of particle size: 2 and  $0.7 \mu\text{m}$ . The  $\text{Li}_{0.5}\text{In}$  counter electrode was prepared by mixing Li (FMC Lithium Corp.) and In (Sigma-Aldrich, 99.99%) powder in the atomic ratio of 0.5:1 and compressing them in contact with the SE pellet during cell assembly. Poly(*tert*-butyl acrylate) (TBA) with a number-average molecular weight ( $M_n$ ) of  $143\,000 \text{ g mol}^{-1}$  and poly(*tert*-butyl acrylate)-*b*-poly(1,4-butadiene) (TBA-*b*-BR) in which the TBA and BR blocks have  $M_n$  values of  $20\,000$  and  $130\,000 \text{ g mol}^{-1}$ , respectively, were purchased from Polymersource Inc. Polybutadiene rubber with a weight-average molecular weight ( $M_n$ ) of  $\approx 200\,000 \text{ g mol}^{-1}$  was purchased from Sigma-Aldrich.

**Characterization of Materials:** The thermal behavior of the deprotection reaction was monitored by thermogravimetric analysis (TGA, Q500, TA Instruments). The thermograms of binders were obtained using DSC (DSC 4000, Perkin-Elmer). The characteristics of the chemical bonds of the TBA and TBA-*b*-BR binders before and after deprotection were analyzed by FT-IR (Tensor27, Bruker). The compatibility of the LPSCI SE with the binders was assessed by dispersing the LPSCI powder in 2.5 wt% binder solutions based on butyl butyrate and dried at  $120 \text{ }^\circ\text{C}$  for 15 h. The same procedure was followed for the deprotected binders except that the drying temperature was raised to  $160 \text{ }^\circ\text{C}$ . After the drying step, the crystal structures and bonding characteristics of the LPSCI were examined by performing XRD analysis (New D8 Advance, Bruker) and Raman spectroscopy (Raman, DXR2xi, Thermo), respectively. The peeling strength of the composite cathodes was evaluated by conducting a  $180^\circ$  peeling test using a universal testing machine (QM 100S, QMESYS). For this test, 3M scotch tape was attached to the electrode of  $25 \times 30 \text{ mm}^2$  and was peeled off at a constant displacement rate of  $10 \text{ mm s}^{-1}$  while the peeling force was continuously monitored. For mandrel tests, composite cathodes were prepared and were subjected to five bending–unbending cycles around the cylindrical mandrels with varying diameters (3–8 mm). The cross-sectional images of the composite cathode layers before and after cycling were obtained using a FIB (Helios G4, Thermo Fisher Scientific). The cross-sectional images of the NCM/graphite full-cell were obtained using plasma focused ion beam (Helios G4 PFIB CXe Dual Beam, FEI Company).

**Electrochemical Characterization:** The Li ionic conductivities were measured by AC impedance analysis using a battery cyler (VSP, Bio-Logic). For this analysis, slurries containing the LPSCI electrolyte and binders in a weight ratio of 97.5:2.5 were prepared in butyl butyrate, dried completely, and then pelletized at 590 MPa. AC impedances were then measured in a symmetric cell configuration of Al foil|LPSCI-binder composite layer|Al foil in the frequency range from 1 MHz to 0.1 Hz. The obtained impedance profiles were fitted to the equivalent circuit using the Z-view software. The ionic conductivity was determined by using the following relation:  $\sigma = L/R_b A$ , where  $L$ ,  $R_b$ , and  $A$  correspond to the thickness of the LPSCI electrolyte layer, the bulk resistance, and the area of the LPSCI electrolyte layer, respectively. The electrochemical stability of the (deprotect) TBA-*b*-BR binder was examined by CV measurement in which the voltage was scanned at 0.1 mV s<sup>-1</sup> in the potential range of 1.5–3.7 V versus Li–In. The binder films used in this analysis were prepared by casting 10 wt% binder solutions based on butyl butyrate onto Al foil followed by heat treatment at 160 °C for 15 h. For the fabrication of the all-solid-state half-cells, the composite cathodes were prepared by first dispersing NCM711, LPSCI, super P, and binder in butyl butyrate in a weight ratio of 74.5:21.5:2:2, followed by casting on Al foil and drying at 120 °C for 15 h. The binders were deprotected by subjecting the electrodes to heat treatment at 160 °C for 15 h for in situ deprotection and then maintained at room temperature under vacuum for 24 h. The cell assembly was fabricated by first pelletizing 100 mg of LPSCI to the SE layer by cold-pressing it at 120 MPa, followed by positioning the composite cathode layer underneath the SE layer. The anode layer composed of Li<sub>0.5</sub>In was then placed on top of the SE layer. Subsequently, the assembled cell was compressed at pressure of 590 MPa. Al and Cu foils were used as the cathode and anode current collectors, respectively. After the compression, the cell was positioned in a housing case that was internally fabricated for pressure control during cell testing. The torque applied during cell tests was 12 Nm. The electrochemical performance of the all-solid-state half-cells was galvanostatically assessed in the potential range of 1.88–3.68 V versus Li–In using a battery cyler (MACCOR series 4000). Both the charge and discharge were proceeded in constant current constant voltage (CCCV) mode, and the C-rate was defined as 1C = 195 mA g<sup>-1</sup>. The NCM711/graphite all-solid-state full-cells were fabricated by preparing the composite cathode electrodes via the same procedure as for the half-cells. Electrolyte slurries consisting of LPSCI and BR binder in butyl butyrate in a weight ratio of 97.5:2.5 were cast onto the completely dried cathode layer, followed by heat treatment at 160 °C for 15 h. Anode slurries were prepared by dispersing graphite, LPSCI, and BR binder in butyl butyrate in a weight ratio of 78:19.5:2.5 and were cast onto Ni foil using the doctor blade technique, followed by heat treatment at 120 °C for 1 h and subsequent drying at room temperature under vacuum for 24 h. The cell was assembled by placing the composite anode layer on the LPSCI-cathode assembly and compressed at 490 MPa. The n/p ratio (the areal capacity ratio between the negative and positive electrodes) was 1.2. After compression, the cell was positioned in the same housing case as in the half-cell tests. All assembly processes were carried out in an Ar-filled glove box.

## Supporting Information

Supporting Information is available

## Acknowledgements

The authors acknowledge financial support from a National Research Foundation of Korea grant (NRF-2017M1A2A2044504) and generous support from the Institute of Engineering Research (IER) at Seoul National University.

## Conflict of Interest

The authors declare no conflict of interest.

## Keywords

acrylate polymers, argyrodite, polarity switching, protection–deprotection chemistry, thermolysis

- [1] a) M. Armand, J.-M. Tarascon, *Nature* **2008**, *451*, 652; b) J. B. Goodenough, Y. Kim, *Chem. Mater.* **2010**, *22*, 587.
- [2] a) Y. Seino, T. Ota, K. Takada, A. Hayashi, M. Tatsumisago, *Energy Environ. Sci.* **2014**, *7*, 627; b) Y. Wang, W. D. Richards, S. P. Ong, L. J. Miara, J. C. Kim, Y. Mo, G. Ceder, *Nat. Mater.* **2015**, *14*, 1026; c) M. Tatsumisago, M. Nagao, A. Hayashi, *J. Asian Ceram. Soc.* **2013**, *1*, 17.
- [3] a) A. Manthiram, X. Yu, S. Wang, *Nat. Rev. Mater.* **2017**, *2*, 16103; b) S. Wenzel, D. A. Weber, T. Leichtweiss, M. R. Busche, J. Sann, J. Janek, *Solid State Ionics* **2016**, *286*, 24; c) K. H. Park, Q. Bai, D. H. Kim, D. Y. Oh, Y. Zhu, Y. Mo, Y. S. Jung, *Adv. Energy Mater.* **2018**, *8*, 1800035.
- [4] N. Kamaya, K. Homma, Y. Yamakawa, M. Hirayama, R. Kanno, M. Yonemura, T. Kamiyama, Y. Kato, S. Hama, K. Kawamoto, *Nat. Mater.* **2011**, *10*, 682.
- [5] Y. Kato, S. Hori, T. Saito, K. Suzuki, M. Hirayama, A. Mitsui, M. Yonemura, H. Iba, R. Kanno, *Nat. Energy* **2016**, *1*, 16030.
- [6] a) S. Boulineau, M. Courty, J.-M. Tarascon, V. Viallet, *Solid State Ionics* **2012**, *221*, 1; b) C. Yu, L. van Eijck, S. Ganapathy, M. Wagemaker, *Electrochim. Acta* **2016**, *215*, 93; c) H. J. Deiseroth, S. T. Kong, H. Eckert, J. Vannahme, C. Reiner, T. Zais, M. Schlosser, *Angew. Chem., Int. Ed.* **2008**, *47*, 755; d) J. Auvergniot, A. Cassel, J.-B. Ledeuil, V. Viallet, V. Seznec, R. m. Dedryvère, *Chem. Mater.* **2017**, *29*, 3883; e) C. Yu, S. Ganapathy, N. J. J. de Klerk, I. Roslon, E. R. H. van Eck, A. P. M. Kentgens, M. Wagemaker, *J. Am. Chem. Soc.* **2016**, *138*, 11192.
- [7] J. Schnell, T. Günther, T. Knoche, C. Vieider, L. Köhler, A. Just, M. Keller, S. Passerini, G. Reinhart, *J. Power Sources* **2018**, *382*, 160.
- [8] a) K. Lee, S. Kim, J. Park, S. H. Park, A. Coskun, D. S. Jung, W. Cho, J. W. Choi, *J. Electrochem. Soc.* **2017**, *164*, A2075; b) K. Lee, J. Lee, S. Choi, K. Char, J. W. Choi, *ACS Energy Lett.* **2019**, *4*, 94; c) T. Inada, K. Takada, A. Kajiyama, M. Kouguchi, H. Sasaki, S. Kondo, M. Watanabe, M. Murayama, R. Kanno, *Solid State Ionics* **2003**, *158*, 275; d) A. Sakuda, K. Kuratani, M. Yamamoto, M. Takahashi, T. Takeuchi, H. Kobayashi, *J. Electrochem. Soc.* **2017**, *164*, A2474; e) D. Y. Oh, D. H. Kim, S. H. Jung, J.-G. Han, N.-S. Choi, Y. S. Jung, *J. Mater. Chem. A* **2017**, *5*, 20771; f) M. Yamamoto, Y. Terauchi, A. Sakuda, M. Takahashi, *Sci. Rep.* **2018**, *8*, 1212; g) Y. J. Nam, D. Y. Oh, S. H. Jung, Y. S. Jung, *J. Power Sources* **2018**, *375*, 93; h) T. Ates, M. Keller, J. Kulisch, T. Adermann, S. Passerini, *Energy Storage Mater.* **2019**, *17*, 204; i) J. Zhang, H. Zhong, C. Zheng, Y. Xia, C. Liang, H. Huang, Y. Gan, X. Tao, W. Zhang, *J. Power Sources* **2018**, *391*, 73.
- [9] D. H. Tan, A. Banerjee, Z. Deng, E. A. Wu, H. Nguyen, J.-M. Doux, X. Wang, J.-h. Cheng, S. P. Ong, Y. S. Meng, *ACS Appl. Energy Mater.* **2019**, *2*, 6542.
- [10] N. Riphaut, P. Strobl, B. Stiaszny, T. Zinkevich, M. Yavuz, J. Schnell, S. Indris, H. A. Gasteiger, S. J. Sedlmaier, *J. Electrochem. Soc.* **2018**, *165*, A3993.



- [11] S. Ito, S. Fujiki, T. Yamada, Y. Aihara, Y. Park, T. Y. Kim, S.-W. Baek, J.-M. Lee, S. Doo, N. Machida, *J. Power Sources* **2014**, *248*, 943.
- [12] N. C. Rosero-Navarro, T. Kinoshita, A. Miura, M. Higuchi, K. Tadanaga, *Ionics* **2017**, *23*, 1619.
- [13] P. Bisel, L. Al-Momani, M. Müller, *Org. Biomol. Chem.* **2008**, *6*, 2655.
- [14] N. D. Treat, N. Ayres, S. G. Boyes, W. J. Brittain, *Macromolecules* **2006**, *39*, 26.
- [15] a) Y. Shi, X. Zhou, G. Yu, *Acc. Chem. Res.* **2017**, *50*, 2642; b) A. Magasinski, B. Zdyrko, I. Kovalenko, B. Hertzberg, R. Burtovyy, C. F. Huebner, T. F. Fuller, I. Luzinov, G. Yushin, *ACS Appl. Mater. Interfaces* **2010**, *2*, 3004.
- [16] a) Y.-H. La, E. W. Edwards, S.-M. Park, P. F. Nealey, *Nano Lett.* **2005**, *5*, 1379; b) J. Y. Kelly, J. N. Albert, J. A. Howarter, S. Kang, C. M. Stafford, T. H. Epps III, M. J. Fasolka, *ACS Appl. Mater. Interfaces* **2010**, *2*, 3241; c) J. Schaeffgen, I. Sarasohn, *J. Polym. Sci., Part A: Polym. Chem.* **1962**, *58*, 1049.
- [17] a) J. Duvigneau, S. Cornelissen, N. Bardají Valls, H. Schönherr, G. J. Vancso, *Adv. Funct. Mater.* **2010**, *20*, 460; b) J. Duvigneau, H. Schönherr, G. J. Vancso, *Langmuir* **2008**, *24*, 10825.
- [18] S. Yubuchi, M. Uematsu, M. Deguchi, A. Hayashi, M. Tatsumisago, *ACS Appl. Energy Mater.* **2018**, *1*, 3622.
- [19] S. Yubuchi, S. Teragawa, K. Aso, K. Tadanaga, A. Hayashi, M. Tatsumisago, *J. Power Sources* **2015**, *293*, 941.
- [20] a) J. He, L. Zhang, *J. Alloys Compd.* **2018**, *763*, 228; b) J. Chong, S. Xun, H. Zheng, X. Song, G. Liu, P. Ridgway, J. Q. Wang, V. S. Battaglia, *J. Power Sources* **2011**, *196*, 7707.
- [21] a) Y. Zhu, X. He, Y. Mo, *ACS Appl. Mater. Interfaces* **2015**, *7*, 23685; b) S. Wenzel, S. J. Sedlmaier, C. Dietrich, W. G. Zeier, J. Janek, *Solid State Ionics* **2018**, *318*, 102; c) S. H. Kim, K. Char, S. I. Yoo, B. H. Sohn, *Adv. Funct. Mater.* **2017**, *27*, 1606715; d) W. Zhang, F. Richter, S. P. Culver, T. Leichtweiß, J. G. Lozano, C. Dietrich, P. G. Bruce, W. G. Zeier, J. Janek, *ACS Appl. Mater. Interfaces* **2018**, *10*, 22226.
- [22] a) R. Koerver, I. Aygün, T. Leichtweiß, C. Dietrich, W. Zhang, J. O. Binder, P. Hartmann, W. G. Zeier, J. Janek, *Chem. Mater.* **2017**, *29*, 5574; b) R. Koerver, W. Zhang, L. de Biasi, S. Schweidler, A. O. Kondrakov, S. Kolling, T. Brezesinski, P. Hartmann, W. G. Zeier, J. Janek, *Energy Environ. Sci.* **2018**, *11*, 2142; c) F. Walther, R. Koerver, T. Fuchs, S. Ohno, J. Sann, M. Rohnke, W. G. Zeier, J. Janek, *Chem. Mater.* **2019**, *31*, 3745.
- [23] J. Zhang, C. Zheng, L. Li, Y. Xia, H. Huang, Y. Gan, C. Liang, X. He, X. Tao, W. Zhang, *Adv. Energy Mater.* **2020**, *10*, 2070017.
- [24] Z. Zhang, L. Zhang, Y. Liu, C. Yu, X. Yan, B. Xu, L.-M. Wang, *J. Alloys Compd.* **2018**, *747*, 227.
- [25] a) A. O. Kondrakov, A. Schmidt, J. Xu, H. Geßwein, R. Mönig, P. Hartmann, H. Sommer, T. Brezesinski, J. Janek, *J. Phys. Chem. C* **2017**, *121*, 3286; b) A. O. Kondrakov, H. Geßwein, K. Galdina, L. de Biasi, V. Meded, E. O. Filatova, G. Schumacher, W. Wenzel, P. Hartmann, T. Brezesinski, *J. Phys. Chem. C* **2017**, *121*, 24381.
- [26] a) Y. Ito, M. Otoyama, A. Hayashi, T. Ohtomo, M. Tatsumisago, *J. Power Sources* **2017**, *360*, 328; b) W. Zhang, D. A. Weber, H. Weigand, T. Arlt, I. Manke, D. Schröder, R. Koerver, T. Leichtweiss, P. Hartmann, W. G. Zeier, *ACS Appl. Mater. Interfaces* **2017**, *9*, 17835; c) J. A. Lewis, J. Tippens, F. J. Q. Cortes, M. T. McDowell, *Trends Chem.* **2019**, *1*, 845.
- [27] a) W. Zhang, D. Schröder, T. Arlt, I. Manke, R. Koerver, R. Pinedo, D. A. Weber, J. Sann, W. G. Zeier, J. Janek, *J. Mater. Chem. A* **2017**, *5*, 9929; b) Z. D. Hood, M. Chi, *J. Mater. Sci.* **2019**, *54*, 10571.